CHARACTERIZATION AND MODELING OF CMOS-COMPATIBLE ACOUSTICAL PARTICLE VELOCITY SENSORS FOR APPLICATIONS REQUIRING LOW SUPPLY VOLTAGES

M. Piotto[a], F. Butti[b], E. Zanetti[c], A. Di Pancrazio[c], G. Iannaccone[c], P. Bruschi[c]

[a]IEIIT-Pisa, CNR, via G. Caruso 16, I-56122, Pisa, Italy

[b]Marvell Semiconductors, viale della Republica 38, I-27100 Pavia, Italy

[c]Dipartimento di Ingegneria dell'Informazione, University of Pisa, via G. Caruso 16, I-56122 Pisa, Italy

Abstract

Acoustic particle velocity sensors have been obtained applying simple low resolution micromachining steps to chips fabricated using a standard microelectronic process. Each sensor consists of four silicided polysilicon wires, suspended over cavities etched into the substrate, and connected to form a Wheatstone bridge. Full compatibility of the micromachining procedure with the original process is demonstrated by integrating a simple pre-amplifier on the same chip as the sensors and showing that both blocks are functional. Proper design of the sensing structures allows them to operate with a single 3.3 V power supply. Sensitivity and noise measurements, performed to estimate the sensor detection limit, are described. Excess noise with a flicker-like behavior, not ascribable to the amplifier, is found when the bridges are biased in working conditions. In addition, the dependence of the sensitivity on the dc bias voltage of the bridges is investigated, comparing the experimental data with the results of a simple analytical model and Finite Element Method simulations.

Keywords: Acoustic particle velocity sensor; CMOS-compatible; integrated chopper pre-amplifier; sensitivity model; excess noise

Corresponding Author:
Massimo Piotto,
IEIIT-Pisa, CNR,
via G. Caruso 16,
I-56122, Pisa, Italy
Tel +39 050 2217657,
Fax +39 050 2217522,
e-mail: massimo.piotto@ieiit.cnr.it

1. Introduction

Microphones are by far the most common type of sensor used for measuring sound; they actually sense sound pressure waves, to which human ears are sensitive too. Pressure, however, is only one of two inseparable physical quantities constituting sound waves: the other one being the local velocity of the transmitting medium (macroscopic) particles. The ratio of pressure to velocity is the so-called acoustic impedance [1]. It is very interesting to notice that, while pressure is a scalar quantity, velocity is a vector, thus described by both a magnitude and a direction. Whenever the approximation of plane wave, or at least spherical wave, is applicable, the direction of the sound particle velocity is immediately related to the propagation direction of sound. By measuring sound velocity instead of pressure is thus straightforward to extract the sound direction of arrival (DOA). This is very useful, just to name a few applications, for sound source localization [2,3] and beam-forming [4,5]. An important case that, in the near future, might justify mass production of DOA detectors is constituted by systems designed to individuate humans requesting attention with vocal commands in order, for example, to steer a video camera in teleconferences or guide a robot for disabled person assistance. A popular alternative method for the DOA determination consists in using an array of two (or more) microphones, and in measuring the sound wave phase difference between them to compute the incoming sound wave inclination with respect to the array axis. This solution, however, cannot be arbitrarily miniaturized due to constraints on the distances between the microphones. Furthermore it is intrinsically narrow-banded and requires strict sensor matching [5,6,7].

For these reasons, over the last few years there has been quite some interest in the development of acoustic particle velocity (APV) sensors; the first effective implementation was proposed by de Bree et al. [8,9], and was based on forced thermal convection between two heated wires. Further development of this sensor has led to more sensitive [10], three-dimensional probes [11] and to a few available commercial products [12]. However, the intrinsically fragile sensor geometry makes them not

sufficiently rugged for some applications; alternative layouts have been more recently proposed [13] in order to improve this aspect. An alternative approach for the development of APV sensors, based on a mechanical principle and inspired by the wind receptor hairs of insects, is detecting the force exerted by the local oscillating airflow on microscopic artificial hairs [14]. This “biomimetic” approach has been demonstrated to be particularly suitable for hydrophone fabrication [15] while, similarly to thermal APV sensors, the critical aspect for application in air is the detection limit, being currently 1 mm/s [16].

Recently, we have demonstrated the possibility of using a CMOS-compatible process to fabricate APV sensors [17] based on the same thermal principle as those in refs [8-13]. Use of a CMOS compatible fabrication flow enables integration of the readout circuits on the same substrate as the sensing structures, improving immunity to electromagnetic interference, an aspect that is critical due to the very low signal levels produced by the thermal APV sensors. Additional advantages of this approach are overall system compactness and, at least for high volume production, cost reduction. These sensors, consisting of two wires arranged in a half-bridge configuration, have been used for fabricating devices with a programmable directivity [18] and compact probes for acoustic impedance measurements [19]. In order to maximize the output voltage, the sensors are biased at nearly constant current, using large series resistors. The current is set to heat the wires up to the maximum temperature that can be reliably withstood by the materials employed. This leads to a larger supply voltage than typically used in modern low-voltage applications.

In this work we propose a novel device that has been specifically designed for low voltage applications. Since the sensitivity is proportional to the static voltage across the wires, we have partially recovered the detection limit degradation caused by low supply voltage by doubling the sensitivity with a full-bridge configuration and lowering the wire resistance in order to reduce thermal noise. The subsequent amplifier needs to be designed in order to match the low-noise characteristics of the sensors; this has been obtained with a CMOS chopper pre-amplifier, integrated on the same die. Pre-amplifier

integration also improves the electromagnetic interference rejection, which may be very significant because of the low output voltage levels of this kind of sensors. Furthermore, successful integration of the pre-amplifier demonstrates the compatibility of the used micromachining process needed for the sensor fabrication with standard Integrated Circuit (IC) technology.

Preliminary experimental characterization of these sensors, demonstrating correct operation of both the sensing elements and the integrated pre-amplifier, were presented in [20]. In this work, we present additional measurements, showing the sensitivity dependence on frequency and sensor orientation. New noise measurements, performed on samples that were not post-processed, are described, in order to add information about the causes of the excess noise observed in operating conditions. Furthermore, the relationship between sensitivity and bias voltage has been thoroughly investigated by means of a lumped element model and numerical simulations. This aspect is particularly important, since increasing the bias voltage up to the maximum value that can be reliably withstood by the sensor is the principal method to maximize the sensitivity. Unfortunately, experimental data show that the large sensitivity increments that can be envisioned on the basis of intuitive considerations (see end of Sect.3.3) or first order approximations (see Sect. 4.1) are widely overestimated. The causes of this discrepancy were investigated by means of Finite Element simulations.

2. Device description and fabrication

2.1. Principle of operation

Similarly to the already cited Microflown [8,9,10] (specifically the two sensor microflown, TSM), the proposed sensor is based on a pair of parallel electrically conducting wires of micrometric cross-section immersed in the medium (typically air) where the acoustic waves to be detected propagate. The wires are heated by an electrical current as large as to produce an overheating of up to a few hundreds Kelvin with respect to surrounding air (static overheating). Thermal coupling between the wires occurs through the micrometric air gap that separates them.

In absence of any externally imposed air flow, the surrounding air reaches a steady state temperature profile which is qualitatively shown in Fig. 1 (solid line). When an air flow is added, its effect simply consists in deforming the temperature distribution (dashed line in Fig.1) in the direction of the fluid velocity, as a result of convective heat transfer (forced convection). In this perturbed state, the two wires are in contact with air at different temperatures, so that a temperature difference between them is generated. In the case of an oscillating air flow stimulus (e.g. a sound wave) the overheating profile of air simply oscillates back and forth, and so does the temperature difference between the two wires. This temperature difference induces a proportional resistance variation, through the temperature coefficients of resistance (TCR) of the wires. The resistance difference, for typical sound intensities of practical interest, can be considered a small signal perturbation. For the steady state resistance value R_T of the wires we can write

$$R_T = R_0[1 + \alpha(T - T_0) + \beta(T - T_0)^2] \quad (1)$$

where α and β are, respectively, the first and second order temperature coefficients, and R_0 is the resistance at the reference temperature T_0 , which we have assumed to be the room temperature, to simplify calculations. The small signal temperature perturbation δT, caused by the air flow, produces an infinitesimal resistance variation, $\delta R = R_0[\alpha + 2\beta(T - T_0)] \cdot \delta T$, which can be added to the quiescent (hot) resistance as

$$R_{perturbed} = R_T \pm \delta R \quad (2)$$

where the presence of both signs represents the fact that, due to the symmetry of the sensor, when one resistance experiences a negative value variation, the other experiences a positive one, and vice-versa. Detection of the resistance variation allows measurement of the instantaneous local air velocity. This principle has been used for a long time to detect the intensity and direction of static or slowly varying flow (mass flow sensors). Reduction of the wire dimensions to the micrometric range causes a significant reduction of the thermal masses, extending the operating frequency up to the audio range.

2.2. Sensor layout and fabrication

The sensor layout presents important differences with respect to previous works [8,9,13]. In the proposed device, the wires have been split into different short segments, sustained by U-shaped silicon dioxide membranes suspended over cavities etched into the bulk silicon. By this approach, the wire robustness is improved and the etching times required to open the cavities are short enough to be applicable as post-processing steps to chips fabricated with standard IC technologies. A schematic perspective representation of the sensing structure is shown in Fig. 2 (a). The two wires are made up of titanium silicide polysilicon (Ti-Si), which is a material commonly available in many CMOS processes. Titanium silicide polysilicon has a relatively high temperature coefficient [21], which, in the process used in this work, was about 3×10^{-3} K^{-1}; the second order coefficient, indicated with β in Eq. (1), was of the order of -8×10^{-7} K^{-2}. The wires are formed by distinct (Ti-Si) lines, placed on the longest side of the U-shaped membranes. The other two sides of the membranes support aluminum interconnections to the wire terminals. The first interconnection layer of the process (Metal 1) is used for this purpose. Each wire is composed of three sections, connected in parallel and placed in such a way that each section of one wire is thermally coupled to a corresponding section of the other wire. The dimensions of two coupled sections are indicated in Fig. 2(b).

Due to the parallel connection, the required bias voltage of a wire is the same as that of each one of the composing sections. This is an advantage in terms of low voltage operation with respect to the series connection used in [17], but does not imply any sensitivity improvement with respect to using a single section. However, connecting multiple sections in parallel reduces the output resistance of the sensor and then lowers the output thermal noise, improving the Signal-to-Noise Ratio (SNR). In [17] the wires were biased with a constant current and the resistance variations were detected by monitoring the voltage variations. In order to approximate the condition of constant current, the wires were placed in series with auxiliary resistors whose value was much higher than the sensor one. This further

exacerbated the need of a high power supply voltage (up to 40 V). In this work, we connected two distinct wire pairs in order to form a Wheatstone full-bridge configuration. As it will be shown in Subsec. 2.3, this allows obtaining a constant current condition with a power supply voltage which is only twice the required bias voltage of a single wire, resulting well within the typical supply voltage used in modern analog ICs. The resistance of a single wire section was set to 321 Ω by design, so that each wire has a resistance of 107 Ω at room temperature.

The chip has been designed with the BCD6s process of STMicroelectronics and simple post-processing steps were applied to thermally insulate the sensing structures from the substrate. The post-processing phase is similar to that described in detail in [17] and the main steps are schematically shown in Fig. 3. Briefly, after the passivation opening performed by the silicon foundry, the dielectric layers in the front side of the chip were selectively removed with reactive ion etching (RIE) in CF4 / Ar (50% / 50%) gas mixture. As far as the RIE mask is concerned, the selectivity of CF4 plasma towards aluminum has been used to define the U-shaped membrane using the second metal layer (Metal 2), as shown in Fig 3(a). In this way we have obtained two positive effects. First, the Metal 2 mask is aligned during the chip layout design and fabricated by the silicon foundry, relaxing the resolution requirement of the post-processing lithography. Second, all the dielectric layers above the Metal 2 are removed (see Fig. 3(b)) reducing the mass of the suspended dielectric membranes with clear advantages in terms of frequency response of the device. Note that aluminum can be used to mask RIE exclusively in the membrane area where electrical interconnections are made only with the first metal layer (Metal 1). Outside the cavity, all the metal layers are used for interconnections and so thick photoresist has been used to define the cavity borders and protect the remaining chip area. After the RIE, the Metal 2 and the photoresist masks have been removed and the silicon substrate has been anisotropically etched in a solution of 100 g of 5 wt% TMAH with 2.5 g of silicic acid and 0.8 g of ammonium persulfate, as schematically shown in Fig. 3b.

In Fig. 4 a SEM micrograph of the full bridge structure after post-processing is shown: the U-shaped membranes are suspended over a cavity with a depth of about 25 μm.

2.3. Biasing strategy

The sensor full-bridge ($W_{1,4}$ of Fig. 5) and the two biasing resistors R_B are connected to the ideal voltage source V_{dd}. In absence of any input (null local fluid velocity) and ignoring any mismatch between the resistors, the resulting voltage on the bridge is

$$V_{bridge} = \frac{R_T}{R_T + 2R_B} V_{dd} \tag{3}$$

where R_T is the resistance assumed by the single wire at the working temperature T.

The series resistances R_B are required in order to lower the available voltage from V_{dd} to a value sustainable by the bridge resistors.

Eq.(3) holds true even when the surrounding air is moving, thus unbalancing the bridge: since the two resistors in each branch of the bridge are arranged as to be influenced by external stimuli with opposite phases (see Fig. 5), the resistance seen from top to bottom of the bridge is always equal to

$$\begin{aligned} R_{bridge} &= (R_1 + R_4)//(R_2 + R_3) = (R_T + \delta R + R_T - \delta R)//(R_T - \delta R + R_T + \delta R) \\ &= R_T \end{aligned} \tag{4}$$

where R_i is the resistance value of the wire W_i.

The consequence is that the current flowing through each resistor of the bridge is constant, and simply equal to

$$I_{res} = \frac{V_{bridge}}{2\,R_T} = \frac{1}{2}\frac{V_{dd}}{R_T + 2R_B} \tag{5}$$

The differential output voltage can then be expressed as $V_{out-bridge} = V_1 - V_2 = 2 \cdot \delta R \cdot I_{res}$.

2.4. Integrated pre-amplifier

A simple but effective low noise pre-amplifier has been integrated on the same chip of the sensors. Use of an integrated pre-amplifier strongly improves immunity to electromagnetic interference, a problem that is particularly serious due to the extremely low level of the sensor output signal.

The preamplifier is a simple n-MOSFET differential pair loaded with polysilicon resistors. Schematic view of the amplifier is shown in Fig. 6 where also the sensor bridge (wires $W_{1\text{-}4}$) and a few external components are shown. The pair is biased by a current (I_{bias}) provided by a simple on-chip block, not shown. Since MOSFETS available in most CMOS process are characterized by very high noise levels (flicker noise) up to frequencies of several kHz, a chopper modulation approach [22] has been applied to reject these noise components. SA_1 and SA_2 chopper modulators are composed by four complementary n-MOSFET-p-MOSFET switches driven by a 200 kHz clock. The clock is produced by a conventional on chip relaxation-type oscillator. The sensor bridge and the pre-amplifier are not directly connected but their terminals are routed to distinct bonding pads. In this way it is possible to independently characterize the pre-amplifier and the sensors. The nominal gain of the pre-amplifier is 28, sufficient for making the noise contribution of subsequent amplification stages (off-chip) negligible. Connection between the two blocks is obtained by means of external conductors. In addition, a few external components are required for correct operation of the circuit: C_{LP} are used to reduce the typical high frequency chopper byproducts (e.g. chopper ripple), while C_{HP} and R_{HP} form a high pass filter to reject output dc components. The power supply voltage V_{dd} was set to 3.3V.

Differently from the simplified schematic of Fig. 6, two different resistors R_{B1} and R_{B2} are used to bias the bridge. The voltage V_{bridge} is varied by changing the sum R_{B1}+R_{B2}, while tuning of the output common mode voltage of the bridge is also possible by changing the R_{B2}/R_{B1} ratio. This operation is necessary to match the input common mode range of the pre-amplifier which spans from 1.0 to 1.4 V. The maximum voltage applied to the bridge was 2.2 V corresponding to an adsorbed current of 12 mA

and bridge power consumption of nearly 26 mW. Considering that the amplifier supply current is 18 mA, the total power drawn from the 3.3 V voltage source is about 100 mW.

An optical photograph of the sensing structure and amplifier is shown in Fig. 7. Since the pre-amplifier devices are concealed by the planarization dummies placed by the silicon foundry, the amplifier layout was superimposed on the photograph and carefully aligned to the visible structures in order to show the actual area occupied by the electronic circuits. A magnification of the sensor area is shown in the figure.

3. Experimental characterization

3.1. Experimental setup and methods

Measurement of the current vs. voltage curve of the bridges was performed using an HP4145B parameter analyzer to sweep V_{bridge} and acquire the resulting current. The resistance estimated from these curves coincides with the resistance of the individual wire (supposed identical). The temperature of the wires was estimated from the resistance datum by inverting Eq.(1) with the first and second order TCR reported in the process manual for silicided polysilicon. Due to non-uniform temperature distribution along the wire length, this procedures yields the average temperature of the wire.

Measurement of the output signal of the bridge was obtained by connecting it to the on-chip pre-amplifier and reading the pre-amplifier output voltage by means of an analog interface board that performs differential to single-ended conversion and provides an additional voltage gain of 200. A programmable 5^{th} order low pass filter is used to avoid aliasing of the signal before analog-to-digital conversion, performed using a 16 bit 2-channel digitalizer (Pico Technology Ltd, mod. ADC216). In order to measure the sensitivity to the APV, the sensors were placed into a standing wave tube similar to that used in [17], equipped with a loudspeaker driven by a waveform generator (Agilent 33220A). The acoustical intensity in the tube was monitored by means of a reference microphone placed at the end of the pipe, where a condition of maximum pressure (minimum APV) is present at any frequencies.

The output of the APV sensor was considered at frequencies such that the distance between the sensor location and the end of the tube is λ/4, where λ is the acoustic wavelength. At these frequencies the APV at the sensor location is maximum and can be easily calculated from the pressure data measured by the microphone. Varying the sensor to pipe end distance by means of a piston, it is possible to vary the frequencies at which these maxima occurs, enabling dense frequency scans. More details about the measurement set-up can be found in [17]. A series of programs running on a personal computer were used to control all the instruments and automate the measurements. The bias voltage (V_{bridge}) of the bridge was varied by changing resistors R_{B1} and R_{B2}.

The maximum output voltage of the bridge ($V_{out\text{-}bridge}$) measured in the experiment described in this work was 100 μV (peak value) which, on the basis of the considerations made in Sect. 2.3, corresponds to a maximum resistance variation of 8.4 mΩ.

3.2. Noise Measurements

Noise, together with sensitivity, affects the minimum detectable signal, defined as the magnitude (*rms*) of the acoustical particle velocity (u_{min}) for which the SNR is unity. Indicating with v_n the total *rms* noise, referred to the amplifier input (sensing structure output), in the frequency bandwidth of interest, then the detection limit is given by:

$$u_{min} = \frac{v_n}{S} \tag{6}$$

where *S* is the sensitivity of the sensing structure, given by the ratio of the output voltage of the bridge over the input acoustic particle velocity. In order to characterize the noise behavior of the sensing structure and pre-amplifier, a series of noise PSD (Power Spectral Density) measurements have been performed. The results of noise density measurements performed in four different conditions are shown in Fig. 8. All the measurements were referred to the pre-amplifier input. The background noise of the amplifier was measured by shorting its inputs and connecting them to a 1.25 V voltage source (required

common mode voltage). The result, represented by curve (d), is a constant noise density of nearly 2.3 nV/sqrt(Hz) across the whole audio frequency range. The noise density measured with the bridge in normal operating conditions (V_{bridge}=2.2 V) is represented by curve (a). Note that a much larger noise with respect to the amplifier background noise is present. This density is also much larger than the expected thermal noise density of the bridge (1.72 nV/sqrt(Hz)), calculated considering that the wire resistance at the maximum operating temperature (530 K) is equal to R_T= 186 Ω. Furthermore, a flicker-like noise frequency dependence can be observed. Integration of the noise in the bandwidth 50-5000 Hz gives a total input referred noise of nearly 400 nV *rms*.

Further experiments have been performed in order to obtain more information about the origin of the measured excess noise. Curve (c) shows the noise spectrum measured with the bridge connected to the amplifier but with the V_{bridge} diagonal shorted (V_{bridge}=0). In this way the bridge is in thermal equilibrium (no current flows into the sensor wires). Resistors R_B were set to provide the correct common mode voltage to the amplifier. This experiment was aimed at checking if a significant contribution from the amplifier input noise current was present. Note that significant input current noise in chopper amplifier cannot be excluded [23]. The result represented by curve (c) clearly proves that the noise density in this condition is only slightly higher than the amplifier background noise by an amount given by the thermal noise of the bridge resistances at room temperature (1.32 nV/sqrt(Hz)). No significant contribution due to the amplifier input current noise (flowing into the bridge resistances) can be observed. Excess noise could also derive from resistance fluctuations of the wires as suggested by previous studies performed on polysilicon [24] and silicided polysilicon [25] resistors. In order to characterize the noise level of the silicided polysilicon wires used in this work, we have measured the noise produced by a sensing structure present on a chip which was not post-processed, so that a cavity was not created under the wires. The difference with a normal sensing structure is that, due to lack of thermal insulation from the substrate, the wire self-heating is negligible and they can be considered to operate at room temperature. The noise measurement was performed by applying a bridge voltage of

2.2 V, as in the case of curve (a). The noise density measured in this way is represented by curve (b). Note that no excess noise with the respect to the case of unbiased bridge can be observed, except for the presence of a small flicker component below 100 Hz. The preliminary conclusion that can be drawn at this stage is that the excess noise measured from the sensors in operating condition does not come from the amplifier and is not a property exhibited at room temperature by the material used for the wires.

3.3. Sensitivity measurements

These measurements were devoted to characterize the dependence of the sensitivity on various parameters of interest. Fig. 9 shows the sensitivity dependence on frequency, together with the frequency response of the system used to read the signals, including the preamplifier, providing a total gain of 5600 (75 dB). The roll-off frequency of the anti-alias filter was set to 10 kHz. The frequency response of the sensors was limited to the range 145 Hz – 4.5 kHz, dictated by the dimensions of the standing wave tube used in the experiments. Sensitivity data are normalized with respect to the value at 855 Hz. Note that the frequency response of the measurement system is nearly flat below 5 kHz, therefore the sensitivity dependence on frequency can be wholly ascribed to the sensors. The sensitivity drop at high frequency is probably due to the thermal mass of the wires, while the decrease at low frequency could derive from the boundary layer dependence on frequency, which was also believed to be the cause of the band-pass behavior of airflow sensors based on hair deflection [26].

The dependence of the normalized sensitivity (magnitude) on the angle formed with the APV direction, considered parallel to the standing wave tube longitudinal axis, is shown in Fig. 10 for two frequencies, namely 530 Hz and 855 Hz, at which the APV exhibits a maximum for a sensor to pipe end distance of 50 cm. A typical figure-of-eight can be clearly observed. Comparison with a cosine dependence shows an excellent agreement, indicating that the sensor output is proportional to the APV component along its axis of maximum sensitivity.

The dependence of the sensor sensitivity with respect to the bias voltage V_{bridge} is shown in Fig.11 at 530 Hz and 855 Hz. The axis of maximum sensitivity of the sensor was aligned to the tube axis in these experiments. Measurements of the sensitivity and average wire static overheating (ΔT) as a function of V_{bridge} are shown in Fig. 11; note that static voltage across a single wire is $V_{bridge}/2$. The temperature was estimated using the procedure described in Sec. 3.1.

Note that the sensitivity is the most critical parameter for this type of sensors: applying Eq. (6) with the maximum sensitivity in Fig. 11 (around 10^{-3} $Vm^{-1}s$) and the *rms* noise reported in Sec. 3.2, the detection limit is 4×10^{-4} m/s. The corresponding acoustic intensity is 78 dBa, a value much higher than the typical intensity of human voice during conversations (60 dBa [27]). Thus, considering Fig. 11, it is desirable to increase the bias voltage until the maximum allowed temperature is reached. We have found that, considering a room temperature of 300 K, the average overheating should not exceed 250 K to avoid permanent resistance changes and eventually failure of one of the bridge arms. Note that thermal runaway phenomena may be responsible of failure at temperature well below the melting point of the structural materials. Furthermore, it should be observed that the overheating shown in Fig.11 is the average value along the wire length, while the maximum value, occurring in the wire middle point, is nearly 28 % higher, (see Sect. 4.2). With an average overheating of 250 K, a maximum overheating of 320 K can be estimated, resulting in a wire temperature of less than 620 K. This is much less than the 880 K value indicated in Ref. [21] as the threshold for permanent damage of titanium silicide resistors. The stability of the material in all the bias conditions reported in this work is confirmed by the fact that no detectable permanent resistance changes were found across several weeks of measurements.

The mechanism by which the bias voltage affects the sensitivity is twofold. First, increasing bias voltage the overheating grows, and so do the temperature gradients, proportionally increasing consequently also the resistance variations δR. Second, the current in the wires increases with V_{bridge}, so that the output signal, proportional to $I_{res}\delta R$, also increases. For moderate overheating, the wire

resistance can be considered still equal to the room temperature value, thus the overheating, which is proportional to Joule power, would increase as the square of V_{bridge}, while the bridge current would be proportional to V_{bridge}. Taking into account both mechanisms, the sensitivity should be proportional to $(V_{bridge})^3$. This behavior is followed only for very low V_{bridge} voltages, while a linear behavior is visible at higher voltages in Fig.11. The practical consequence is that the actual sensitivity gain that can be achieved increasing V_{bridge} are considerably diminished with respect to the prediction of the simple cubic model. This discrepancy is further investigated in the next Section.

4. Analysis of the transduction mechanism

4.1. Lumped element sensitivity model

In order to understand how the sensitivity depends on the bias point, we have developed a lumped element model that employs a first-order linearization approach. Considering θ as the total thermal resistance from one wire to the ambient, the instantaneous wire temperature can be written as:

$$T = T_{amb} + \theta P \tag{7}$$

where P is the total power entering the wire, given by the sum of the Joule heating and external contributions, δP_{ext}, deriving from forced convection terms induced by the acoustic wave. Joule heating is given by:

$$P_J = RI^2 \tag{8}$$

where I and R are the instantaneous current and resistance of the wire.

It is useful to separate the static temperature, equal to $T_{amb}+\Delta T$, where ΔT is the static overheating, from the variation δT induced by the wave. The static overheating is given by:

$$\Delta T = \theta R_T I_{res}^2 \tag{9}$$

where I_{res} is the static current given by Eq.(5). Differentiating Eqs. (7) and (8), we find the following equation, valid for the variations:

$$\delta T = \theta(\delta P_{ext} + I_{res}^2 \delta R) \quad (10)$$

where we have considered that the current through the wire is not affected by the APV, as explained in Subsec.2.3.

Differentiating Eq.(1), we obtain:

$$\delta R = R_0[\alpha + 2\beta\Delta T]\delta T \quad (11)$$

Substituting Eq.(10) into Eq.(11) we can derive δR as a function of δP_{ext}. Considering also that $\delta V = I_{res}\delta R$ we get:

$$\delta V = \frac{[\alpha + 2\beta\Delta T]R_0 I_{res}\,\theta}{1 - [\alpha + 2\beta\Delta T]R_0 I_{res}^2\theta}\,\delta P_{ext} \quad (12)$$

The dependency of δP_{ext} on the bias point is not straightforward. The APV (u_a) produces a perturbation on the temperature distribution that can be considered proportional to u_a [28]. Since the origin of this perturbation is the local oscillatory displacement of the static temperature distribution, larger effects can be expected where the gradients are higher. The perturbation on the temperature profile of the air surrounding the wires produces the δP_{ext} heat flux. Thus, δP_{ext}, whose average over time is zero, can be considered proportional to u_a and to the local temperature gradient. Neglecting the dependence of the air parameters on temperature, heat transfer equations are linear, so that the distribution of the static overheating (equal to $T-T_0$, where T_0 is the room temperature) is everywhere proportional to the stimulus, i.e the total heat generated by the wire (heating power). Due to the linear property of the gradient operator, also the temperature gradient is proportional to the heating power. For the above reasons, we can assume that δP_{ext} is proportional to both u_a and the heating power. Clearly, due to the mentioned linearity, also the wire overheating ΔT (or average overhating for non-uniform temperature distributions along the wire) is proportional to the heating power. For these reasons, δP_{ext} is proportional to the product $u_a\,\Delta T$. Then the following proportionality relationship for the sensitivity can be written:

$$S \equiv \frac{\delta V}{u_a} \propto \frac{[\alpha + 2\beta\Delta T]R_0 I_{res}\,\theta}{1 - [\alpha + 2\beta\Delta T]R_0 I_{res}^2 \theta}\Delta T \tag{13}$$

It is important to notice that this result only shows a factor to which the sensitivity is proportional, thus it is not useful to compute the absolute value of sensitivity. Nevertheless, Eq. (13) can be used to predict the type of dependence of S on V_{bridge}. To this purpose, it is simply necessary to express I_{res} and ΔT as a function of V_{bridge} using Eq. (5) and (9), respectively. For low V_{bridge} values, the overheating is so small that the following relationships are reasonable:

$$|2\beta\Delta T| \ll |\alpha|; \quad [\alpha + 2\beta\Delta T]R_0 I_{res}^2 \theta \ll 1; \quad R_T \cong R_0 \tag{14}$$

Using conditions (14), Eq. (13) can be approximated by:

$$S \equiv \frac{\delta V}{u_a} \;\propto\; \alpha R_0 I_{res}\,\theta\Delta T \cong \alpha R_0^2 \theta^2 I_{res}^3 \;\cong \alpha\theta^2 \frac{V_{bridge}^3}{R_0} \tag{15}$$

This suggests that a proportionality of the sensitivity to V_{bridge}^3 can be expected for low V_{bridge} values. For higher V_{bridge} values, conditions (14) stop being applicable, and the dependence gets more complicate. Numerical evaluation of (13) with substitution (5) and (9), performed with parameters estimated from the experimental data, gives a sensitivity vs V_{bridge} dependence that, even for the highest applied voltages (2.2 V), can be still approximated with a power law such that $S \propto V_{bridge}^{2.3}$.

This result does not explain the data obtained from the actual sensor, in which the sensitivity becomes essentially linear at higher voltages.

A comparison of experimental and analytical data is shown in Fig. 12. Since the analytical sensitivity data lack the appropriate scale factor, we have chosen to determine it by fitting this data to the actual measurements with a least squares method. This has been done only on the initial data points (up to V_{bridge}=0.7 V) since the non-idealities of the sensitivity are less noticeable at low bridge voltages.

4.2. Numerical model

The limited usefulness of the lumped element model was expected, because of the intrinsic difficulty of representing in such a way a complex continuous systems, as the sensor of interest. In order to overcome the limitations of this analytical model, we have developed a FEM model which is able to completely simulate the physics underlying sensor behavior.

The geometry of the sensing structure is essentially three-dimensional; thus, the depth (i.e. the axis parallel to the heater length) cannot be ignored by simply relying on a purely 2D model. Fig. 13 shows the 3D FEM model we have developed with COMSOL software to investigate not only the thermal interaction between the sensing structure and the sound wave but also the mechanical strain of the structure that could contribute to the resistance variation by means of the piezoresistive effect.

First, the deformation of the structure due to the heating has been simulated by applying a constant voltage to the wire and considering the different thermal expansion coefficient values of the materials constituting the sensing structure. The displacement along the vertical direction (z-axis in Fig. 13) resulted greater than those along the other two axes and a maximum value of 20 nm has been obtained in the center of the wire with a bridge voltage of 2.2 V. So, thermal expansion causes deformations that are at least two orders of magnitude less than the minimum dimensions of the structure for the supply voltage values used in this work. In order to investigate also the onset of mechanical oscillations induced by the sound wave, the natural frequency has been calculated both for the structure at room temperature and for the structure stressed by the thermal expansion. In both cases a natural frequency of about 1 Mhz has been obtained, suggesting that oscillations at the audible frequencies can be neglected. Furthermore, mechanical deformations caused by the sound wave can be considered identical for all the wires, since the latter are separated by distances that are negligible with respect to the acoustic wavelength. With this assumption, all the resistors experience the same variations and the Wheatstone bridge remains balanced. All these considerations suggested to us that in our case the mechanical deformations caused by thermal expansion and the sound wave can be neglected,

simplifying the simulation of the thermo-acoustic phenomena. In spite of this simplification, simulating the sensor behavior with a 3D model requires very long simulation times, which is particularly critical for parametric sweeps; moreover, the mesh complexity must be reduced in order to comply with memory limitations, thus reducing accuracy.

Because of these drawbacks, we have tried to find a more efficient, but still reasonably accurate alternative. The solution we have adopted is to introduce the most important depth-related effects as lumped elements of a 2D model, as previously demonstrated in [29]. The depth-dependent quantities, for both stimuli and outputs, are considered as the averages along the "collapsed" direction.

The 3D model is used in order to calculate the steady state operating point (i.e. the static power dissipation) and the magnitude of the heat losses through the lateral suspension beams. The temperature profile along the wire length was found to be nearly parabolic, with a maximum overheating in the middle point which was found to be nearly 28 % higher than the average value. These data are then included as the inputs of another, independent model, which is a 2D section of the sensor; this is shown in Fig. 14. In particular, the average static power dissipation is used as an input heat source, while the heat losses to the substrate through the lateral beams are considered as an out-of-plane heat flux; both of these conditions are imposed on the wire section domains. With these definitions, the wire temperature obtained in the 2D simulations and the average temperature along the wire length predicted by the 3D model, coincides. The validity of the 2D simulations is subordinated to the assumption that the average temperature is also the effective temperature for the conversion from the u_a to δT and hence to δR.

The 2D FEM simulation encompasses three steps:

1. A heat transfer simulation is used to calculate the steady state temperature distribution (i.e. the quiescent point), which is generated by the power dissipated from the wires. Fixed temperature (T_{amb}) boundary conditions (BC) are applied to the edges of air and silicon volumes.

2. An acoustic simulation is run in order to obtain the sound-wave propagation through air; viscous effects near the substrate walls are taken into account, since they are very noticeable because of the small sensor scale (tens of μm). An input sound velocity is imposed on one side wall of the air volume, while the opposite wall has an acoustic impedance BC. The substrate edge is considered a fixed wall and the air volume is taken as infinite in the direction above.
3. A time dependent heat transfer simulation is run, starting from the steady state temperature distribution previously obtained; the air is moved in a sinusoidal fashion with the spatial particle velocity distribution (phase and magnitude) found in the acoustic simulation (output of step2), so that convective heat transfer induced by the acoustic wave is taken into account. The time harmonic temperature oscillations in the wires are finally sampled.

The results provided by the compact 2D COMSOL model for the sensitivity dependence on bridge voltage V_{bridge} are shown in Fig. 15, where the experimental data are also reported for comparison. As it can be seen a good agreement between simulations and measurements has been obtained.

Furthermore the FEM model has been used to investigate the effects which contribute to the sensitivity reduction at higher bridge voltages. The most important effect to be considered is the dependence on temperature of air physical properties, especially the thermal conductivity k and the density ρ.

Thermal conductivity roughly varies from 22 mW/(m·K) at 250 K, to 52 mW/(m·K) at 700 K [30]; because of its increase at higher temperatures, the final overheating reached by the polysilicon wires is lower than what would be expected for constant thermal conductivity. In addition, the increase of the thermal conductivity of air inside the gap that separates the wires increases the contribution of thermal conduction to the heat transfer between the wires. This component, being independent of the air velocity, dampens the temperature difference between the wires, reducing the sensitivity at higher temperature, partly counterbalancing the beneficial effects of a higher temperature of the heaters.

As far as the effect of density is concerned, it can be easily shown that the overheating and, more generally, the static temperature distribution are not affected by this parameter. Nevertheless, since

density affects forced convection heat transfer [31], it is reasonable to expect an influence on the sensitivity.

A comparison of the effects of variable air density and thermal conductivity on the sensitivity, together with the estimate provided by the analytical model and the experimental data is shown in Fig. 16. It is apparent that the reduction of the sensitivity at higher voltages with respect to the simple analytical model is due to both the increase of air thermal conductivity and the reduction of air density.

Conclusions

The experiments shown in this paper demonstrate that the proposed APV thermal sensors, consisting of Wheatstone bridges of thermally coupled wires integrated with a simple low noise pre-amplifier, are capable of operating with a single 3.3 V supply voltage. The proposed fabrication technology uses only inexpensive custom micromachining steps, applied to chips produced with a standard IC technology. This represents a considerable advantage with respect to previously proposed devices that use either a CMOS-incompatible technology or require unconventionally high supply voltages. Noise measurements show that there is considerable excess noise with respect to the expected thermal noise floor. This property, combined with the low sensitivity, gives a detection limit of 78dBa, corresponding to relatively loud sounds. In order to enable applications in real scenarios, a significant improvement of the detection limit is necessary, and this can be accomplished only increasing the sensitivity and, possibly, reducing the noise level. It should be observed that the geometry of proposed devices was not optimized in terms of sensitivity, due to the lack of a simulation tool at the time the chip was designed. Previous work [28], devoted to the optimization of the Microflown, suggests that considerable sensitivity improvements can be obtained by increasing the distance between the wires (L_G). Increasing the length of the wire segments (W_C) and suspending arms (L_C) improves thermal insulation with benefits in terms of sensitivity but requires longer times for the wet etching step. The dimensions of W_C and L_C used in this work are the result of a trade-off between these contrasting issues.

Noise is dominated by a flicker component in the whole frequency range of interest (20 Hz – 10 kHz). Experiments show that the amplifier does not introduce a significant contribution to the excess noise; in addition, the excess noise is also negligible in samples where the wires were not thermally insulated from the substrate, so that their overheating was negligible also when fully biased. The results of these experiments suggest that some thermally activated process should be the cause of the observed excess noise. The only method that could be envisioned so far to reduce the noise level is increasing the number of sections to be connected in parallel, resulting in averaging a larger number of statistically independent noise sources. The drawbacks of this approach are clearly larger area occupation and higher power consumption.

As far as the sensitivity is concerned, the main issue is that the effect of the bias voltage of the bridge is considerably smaller than predicted. Indeed, while a simple lumped element model predicts a power law dependence of the sensitivity on the bias voltage, with an exponent between two and three, only a modest linear behavior is observed in the upper half of the allowed V_{bridge} interval. FEM simulations show that the dependence on temperature of air physical parameters, namely thermal conductivity and density, is the main cause of the observed phenomenon. The satisfactory agreement between the simulated data and experimental results indicates that the developed FEM model can be used for future studies aimed at designing more effective sensing structures.

Aknowledgements

The authors would like to thank the R & D group of the STMicroelectronics of Cornaredo (MI, Italy) for fabrication of the chips described in this work.

References

[1] T. D. Rossing (Ed.), Springer handbook of acoustics, Springer, (2007) 60.

[2] M. Hawkes, A. Nehorai, Wideband source localization using a distributed acoustic vector-sensor array, IEEE Transactions on Signal Processing, 51 (2003) 1479-1491.

[3] H.-E. de Bree, J. Wind, S. Sadasivan, Broad banded acoustic vector sensors for outdoor monitoring propeller driven aircraft, in Proceedings of DAGA, (2010).

[4] M. Hawkes, A. Nehorai, Acoustic vector-sensor beamforming and Capon direction estimation, IEEE Transactions on Signal Processing, 46 (1998) 2291-2304.

[5] Y. I. Wu, K. T. Wong, X. Yuan, S. K. Lau, S. K. Tang, A directionally tunable but frequency-invariant beamformer on an acoustic velocity-sensor triad to enhance speech perception, the Journal of the Acoustical Society of America, 131 (2012) 3891-3902.

[6] J. Kotus, A. Czyżewski, Acoustic Radar Employing Particle Velocity Sensors, in Advances in Multimedia and Network Information System Technologies, Springer Berlin Heidelberg, (2010) 93-103.

[7] H.-E. de Bree, H. te Kulve, Acoustic vector sensors for soldier and compound protection, presented at the 2013 ISL conference, Saint-Louis; France, (2013)

[8] H.-E. de Bree, P. Leussink, T. Korthorst, H. Jansen, T. Lammerink, M. Elwenspoek, The μ-Flown - a novel device measuring acoustical flows, in Proc. of the 8th Int. Conf on Solid-State Sensors and Actuators and Eurosensors IX, (1995), 536-539.

[9] H.-E. de Bree, P. Leussink, T. Korthorst, H. Jansen, T. S. J. Lammerink, and M. Elwenspoek, The μ-flown: a novel device for measuring acoustic flows, Sensors and Actuators A: Physical, 54 (1996) 552-557.

[10] H.-E. de Bree, An overview of microflown technologies, ActaAcustica, 89 (2003) 163-172.

[11] D. R. Yntema, J. W. van Honschoten, R. J. Wiegerink, M. Elwenspoek, A complete three-dimensional sound intensity sensor integrated on a single chip, J. Micromech. Microeng. 18 (2008) 115004-115012.

[12] Microflown Online Product Catalog, [Online]. Available: http://www.microflown.com/

[13] O. Pjetri, R.J. Wiegerink, T.S.J. Lammerink, G.J.M. Krijnen, A crossed-wire 2-dimensional acoustic particle velocity sensor, in Proc. of the IEEE Sensors 2013, (2013), 1-4.

[14] J. Tao, and X. B. Yu, Hair flow sensors: from bio-inspiration to bio-mimicking—a review, Smart Mater. Struct., 21 (2012) 113001 (23pp).

[15] L. Linxian, Z. Wendong, Z. Guojun, and X. Chenyang, Package Optimization of the Cilium-Type MEMS Bionic Vector Hydrophone", IEEE Sensors Journal, 14 (2014), 1185-1192.

[16] H. Droogendijk, C. M. Bruinink, R. G. P. Sanders, A. M. K. Dagamseh, R. JWiegerink and G. J. M. Krijnen, Improving the performance of biomimetic hair-flow sensors by electrostatic spring softening, J. Micromech. Microeng., 22 (2012) 065026 (9pp).

[17] P. Bruschi, F. Butti and M. Piotto, CMOS compatible acoustic particle velocity sensors, Proceedings of IEEE Sensors 2011, Limerick; Ireland, (2011) 1405-1408.

[18] M. Piotto, F. Butti, P. Bruschi, Acoustic velocity sensors with programmable directivity, Lecture Notes in Electrical Engineering, 162 (2014) 271-275.

[19] M. Piotto, A. N. Longhitano, P. Bruschi, M. Buiat, G. Sacchi, D. Stanzial, Design and fabrication of a compact p-v probe for acoustic impedance measurement, Lecture Notes in Electrical Engineering, 268 (2014) 53-56.

[20] M. Piotto, F. Butti, A. Di Pancrazio, P. Bruschi, Low voltage acoustic particle velocity sensor with integrated low noise chopper pre-amplifier, in Proc. of EUROSENSORS 2014, Procedia Engineering, 87 (2014) 736-739.

[21] E. Vereshchagina, R. A. M. Wolters and J. G. E. Gardeniers, The development of titanium silicide–boron-doped polysilicon resistive temperature sensors, J. Micromech. Microeng.21 (2011) 105022 (14pp)

[22] C. C. Enz, G. C. Temes, Circuit techniques for reducing the effects of op-amp imperfections: autozeroing, correlated double sampling, and chopper stabilization, Proceedings of the IEEE, 84 (1996) 1584-1614.

[23] J. Xu, Q. Fan, J. H. Huijsing, C. Van Hoof, R. F. Yazicioglu, K. A. Makinwa, Measurement and Analysis of Current Noise in Chopper Amplifiers, IEEE Journal of Solid-State Circuits, 48 (2013) 1575-1584.

[24] R. Brederlow, W. Weber, C. Dahl, D. Schmitt-Landsiedel, R. Thewes, Low-frequency noise of integrated polysilicon resistors, IEEE Transactions on Electron Devices, 48 (2001) 1180-1187.

[25] J. Raoult, F. Pascal, C. Leyris, I–V and low frequency noise characterization of poly and amorphous silicon Ti-and Co-salicide resistors, Thin Solid Films, 518 (2010) 2497-2500.

[26] M. Dijkstra, J. J. van Baar, R. J. Wiegerink, T. S. J. Lammerink, J. H. de Boer and G. J. M. Krijnen, Artificial sensory hairs based on the flow sensitive receptor hairs of crickets, J. Micromech. Microeng. 15 (2005) S132–S138.

[27] H.-E. de Bree, The Microflown E-Book, Microflown Technologies, (2007) 2-12.

[28] J. W. van Honschoten, V. B. Svetovoy, G. J. M. Krijnen, and M. C. Elwenspoek, Optimization of a Thermal Flow Sensor for Acoustic Particle Velocity Measurements, J. Microelectromechanical Systems, 14 (2005) 436-443.

[29] P. Bruschi, A. Ciomei, M. Piotto, Design and analysis of integrated flow sensors by means of a two-dimensional finite element model, Sensors and Actuators A: Physical, 142 (2008) 153-159.

[30] K. Stephan, and A. Laesecke, The thermal conductivity of fluid air, Journal of physical and chemical reference data 14.1 (1985) 227-234.

[31] F. P. Incropera, Fundamentals of heat and mass transfer, John Wiley & Sons, 6th edition (2005) 355.

Authors Biographies

Massimo Piotto: Massimo Piotto was born in 1970, La Spezia, Italy. He received his laurea degree in Electronic Engineering from the University of Pisa, Italy, in 1996 and his Ph.D. degree in Electronic, Computer and Telecommunication Engineering in 2000. Since December 2001 he has been a researcher of the section of Pisa of the "Istituto di Elettronica e di Ingegneria dell'Informazione e delle Telecomunicazioni" - National Research Council. His main research interests concern micromachining, MEMS, microelectronic and nanoelectronic devices and technologies.

Federico Butti: Federico Butti was born in 1985 in Empoli, Italy. He received the laurea degree in electronic engineering from the University of Pisa, Pisa, Italy, in July 2009. He received the Ph.D. degree in Information Engineering from the University of Pisa in June 2013. He is currently with Marvell Semiconductors, Pavia, Italy. His main area of interest is the design and optimization of analog integrated circuits.

Enrico Zanetti: Enrico Zanetti was born in 1989 in Treviso, Italy, and received the M.Sc. in Electronic Engineering from the University of Pisa in May 2014. He is currently a research fellow at the Department of Information Engineering of the University of Pisa. His main areas of interest are integrated silicon sensors and analog integrated circuits for sensor interfacing.

Alessia Di Pancrazio: Alessia Di Pancrazio earned her Laurea degree in Physics at the University of Pisa, Italy, in 2009 with a thesis on isolation and electrical characterization of a multi-walled carbon nanotube, carried out at the Scuola Superiore Sant'Anna, Pisa, jointly with Rice University, Houston, USA. In 2010 she worked with the Department of Aerospace Engineering, Pisa and she is currently a Research Fellow at the Department of Information Engineering in Pisa. Her main research interests are micro- and nano-devices for biomedical and aeronautical applications.

Giuseppe Iannaccone: Giuseppe Iannaccone is professor of electronics at the University of Pisa, Italy. His research interests include nanoelectronics and quantum transport, design of nanopower analog

integrated circuits, RFID and smart systems. He has published more than 160 papers in peer-reviewed journals and more than 120 papers in proceedings of international conferences, with more than 2500 total citations, according to Scopus.

Paolo Bruschi: Paolo Bruschi was born in Massa, Italy, in 1964. He received the laurea degree in Electronic Engineering from the University of Pisa, Italy, in 1989. In 1993 he joined the Department of Information Engineering as a researcher. He is currently an associate professor of the Department of Information Engineering of the University of Pisa. His main area of interest is the development of integrated silicon sensors and actuators. He is also involved in the design of analog integrated circuits and the development of process simulators.

Figure Captions.

Fig. 1. Qualitative temperature profiles of air along an imaginary straight line (parallel to the x axis) placed just above the sensor heaters. The sections of the wires are drawn for reference. The solid line represents the symmetric steady state overheating with respect to ambient temperature, while the dashed line represents the temperature profile deformation in presence of an air flow in the positive x direction.

Fig. 2. (a) Schematic perspective view of a sensing structure; (b) symbolic layout of two facing wire segments with indication of the main geometrical parameters: W_C=102 μm, W_H=80 μm, L_C=32 μm, L_G=5 μm, L_B=5 μm.

Fig. 3. Schematic view of a cross section of the chip (a) prior to RIE, (b) after the RIE and (c) at the end of the TMAH etching (not to scale)

Fig. 4. SEM micrograph showing the suspended membranes after the silicon etching with a TMAH solution; each wire consists of three sections electrically connected in parallel.

Fig. 5. Electrical schematic of the sensor bridge biasing arrangement.

Fig. 6. Schematic view of the device: the components in the grey boxes (chopper pre-amplifier and wires $W_{1\text{-}4}$, forming the Wheatstone full bridge) are integrated on the chip. The bridge representation reflects the actual position of the wires on the chip, while the topology of the electrical connection is equivalent of that of Fig. 5.

Fig. 7. (a) Optical micrograph of the chip area including the sensing structure and the pre-amplifier; the pre-amplifier layout has been superimposed on the area covered by planarization dummies for clarity. (b) Magnification view of the sensing structure.

Fig. 8. Input referred noise spectral densities in the frequency band 20 Hz – 10 kHz. Curve (a) is the total noise measured with the sensor bridge in operating conditions (V_{bridge}=2.2 V); (b) is the same as (a) but with a sensor not post-processed; (c) is measured with a normal sensor but with V_{bridge}=0; (d) is the amplifier background noise (input shorted).

Fig. 9. Normalized sensor sensitivity (dB) as a function of frequency (top) and frequency response of the readout channel used to interface the sensors, including the integrated pre-amplifier (bottom). The gain drop at 10 kHz is the effect of the anti-alias filter that precedes the digitalizer.

Fig. 10. Polar plot of the normalized sensitivity as a function of the angle formed between the sensor axis of maximum sensitivity and the APV vector, considered coincident with the longitudinal axis of the standing wave tube.

Fig. 11. Sensitivity and average wire overheating as a function of the voltage applied to the bridge. The sensitivity is referred to the bridge output voltage.

Fig. 12. Sensitivity dependence on bridge voltage: comparison between cubic curve, analytical calculation results and experimental measurements. The sensor measurements are relative to a 530 Hz input sound wave. The cubic curve and the analytical results are normalized with a least squares method over the first four data points.

Fig. 13. Axonometric projection of the 3D COMSOL model used for the FEM numerical simulations.

Fig. 14. 2D COMSOL model used for the sensitivity parametric simulations. The figure above is the complete simulation environment, which consists of both the silicon substrate and the surrounding air. The figure below shows a magnification of the sensing structure, with a steady state temperature profile plotted (lines are the isotemperature curves, temperature scale is in Kelvin).

Fig. 15. Sensitivity dependence on bridge voltage: comparison between COMSOL simulation results and experimental measurements.

Fig. 16. Sensitivity dependence on bridge voltage: comparison between analytical model and several COMSOL simulations: a) is the sensitivity obtained from the analytical model; the remaining plots are the results of numerical simulations, with b) constant thermal conductivity and density, c) constant thermal conductivity and variable density, d) variable thermal conductivity and constant density, e) variable thermal conductivity and density. Experimental measurements are also shown.

FIGURES

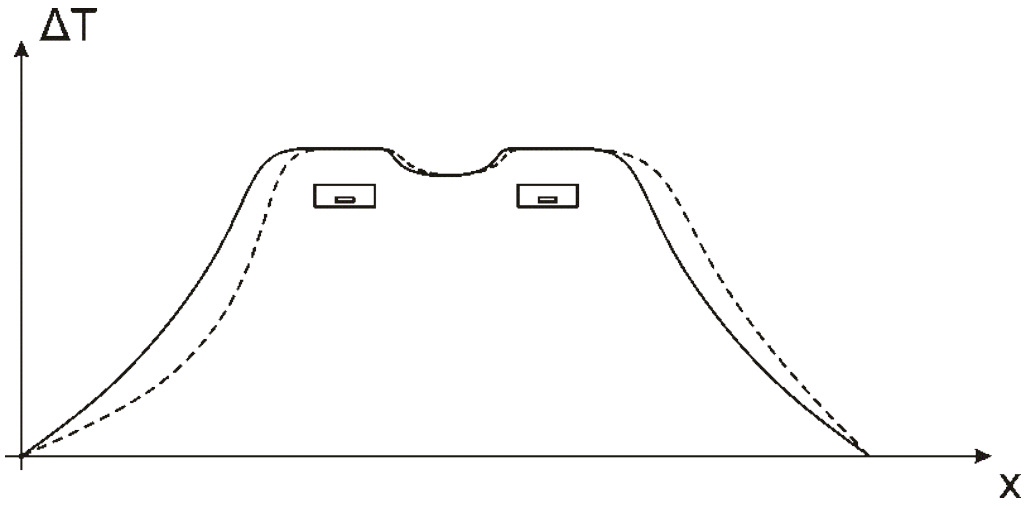

Figure 1

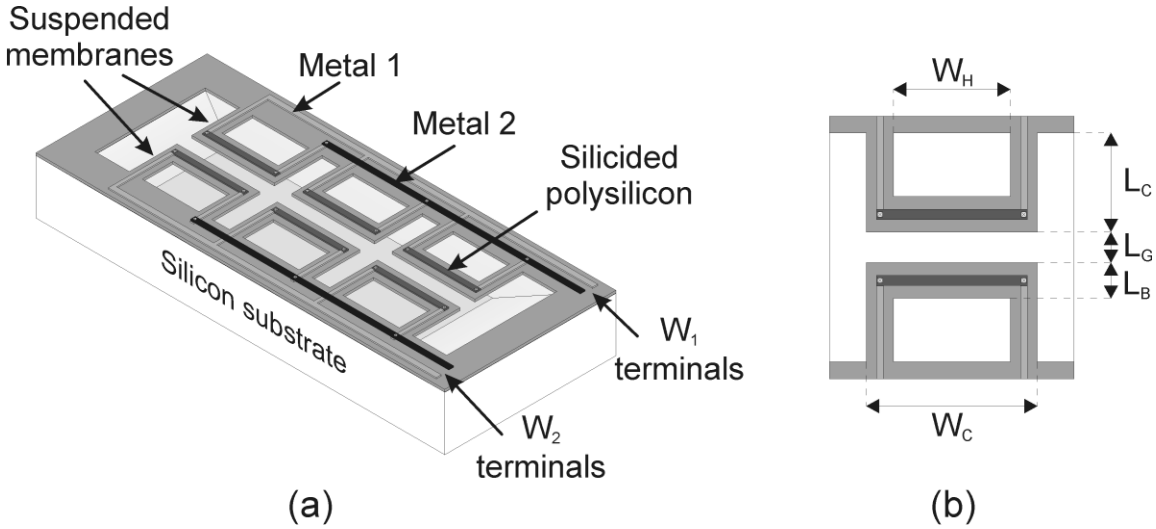

Figure 2

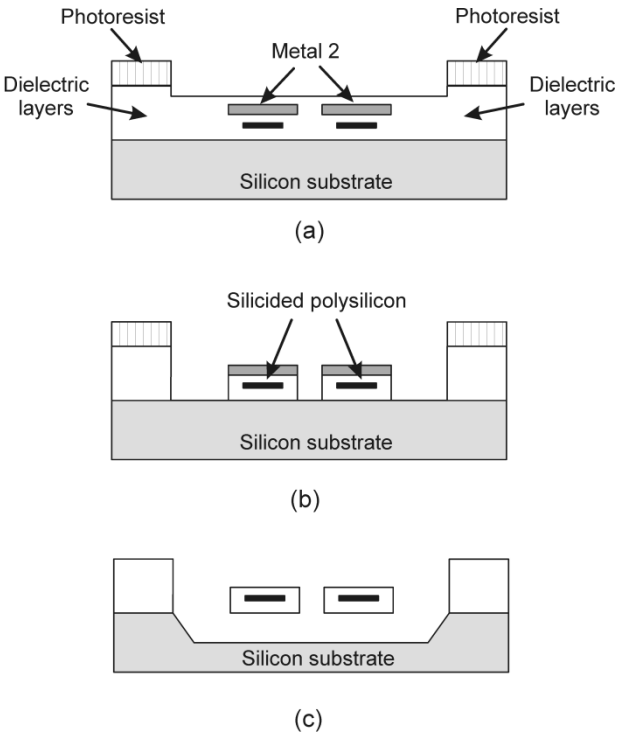

Figure 3

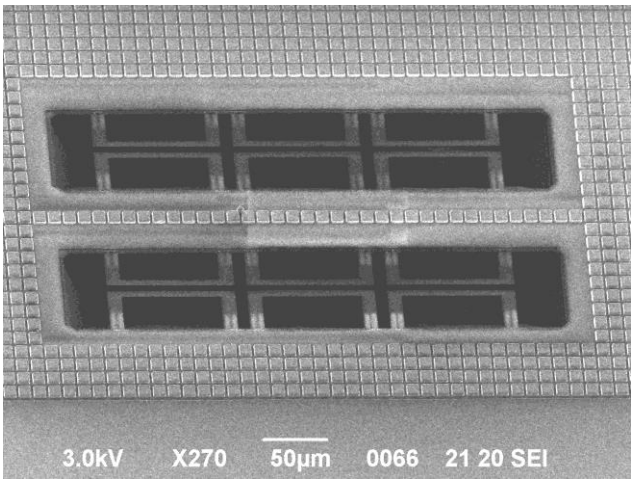

Figure 4

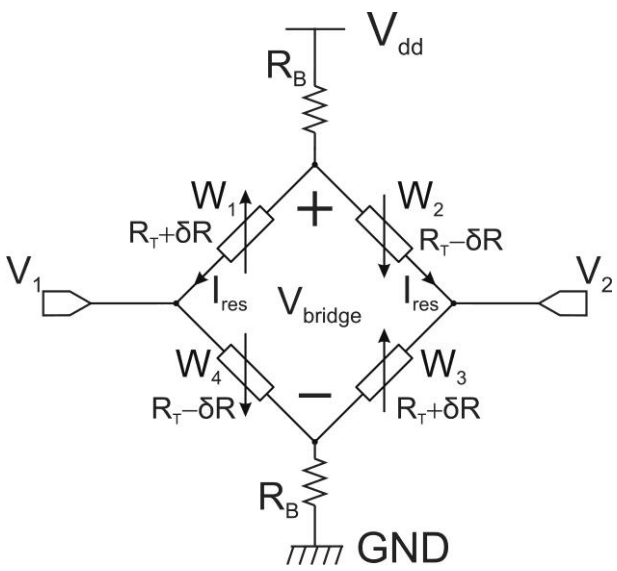

Figure 5

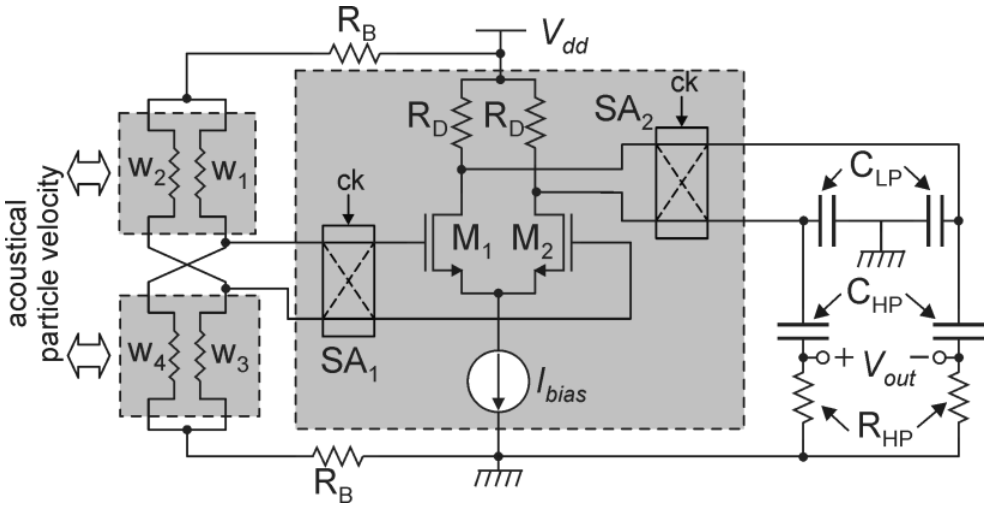

Figure 6

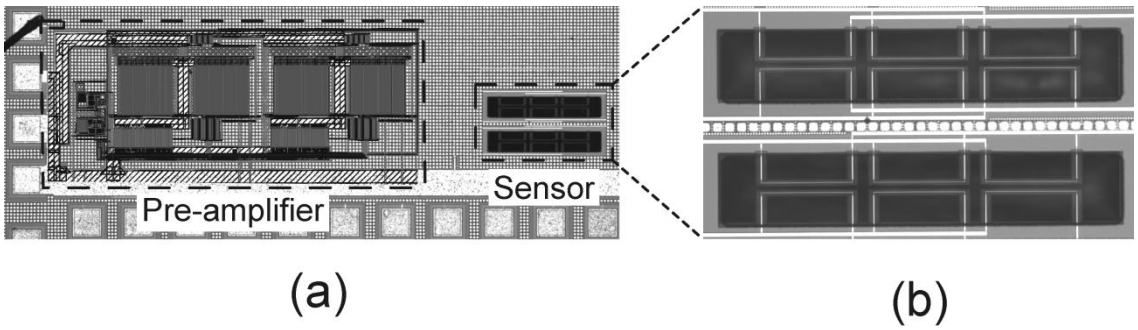

Figure 7

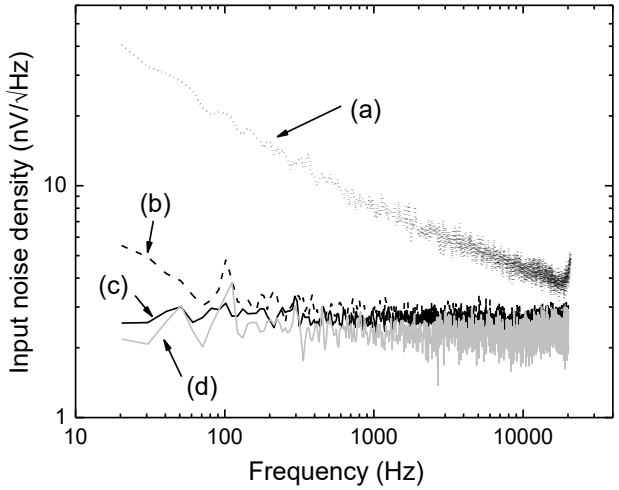

Figure 8

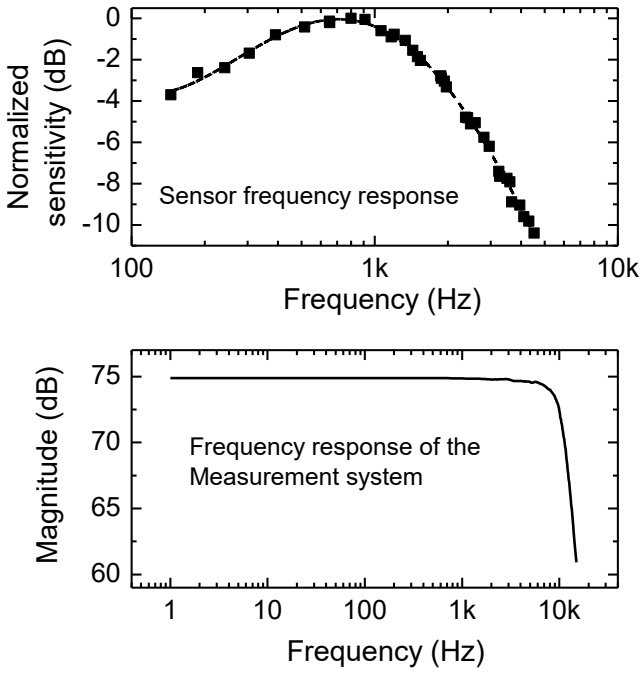

Figure 9

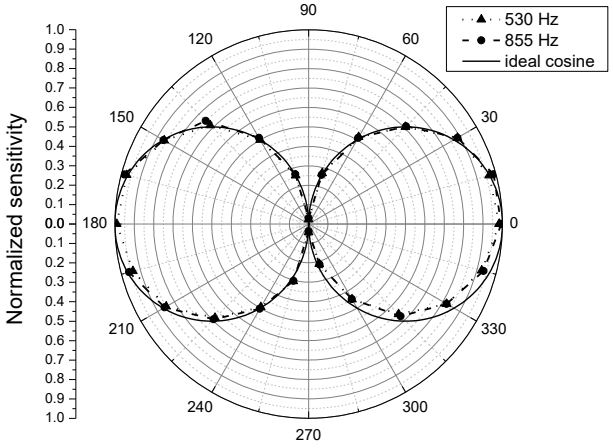

Figure 10

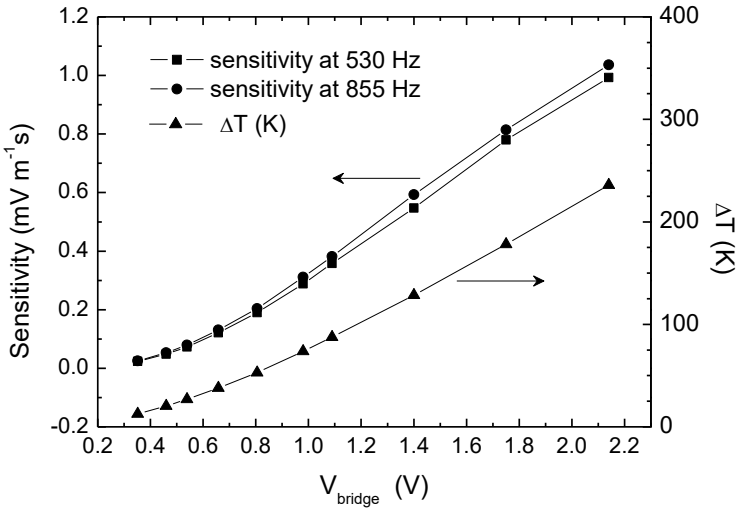

Figure 11

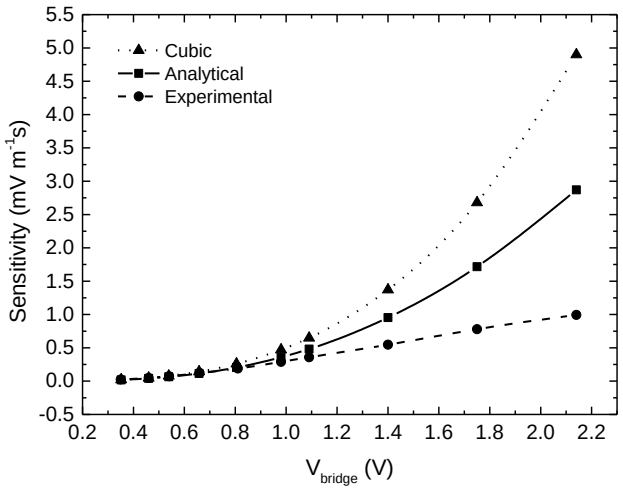

Figure 12

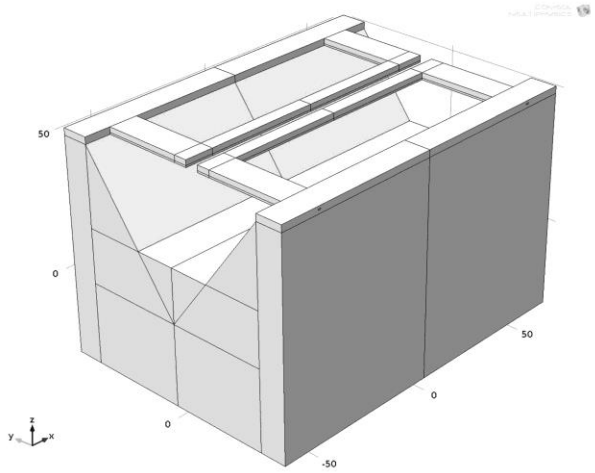

Figure 13

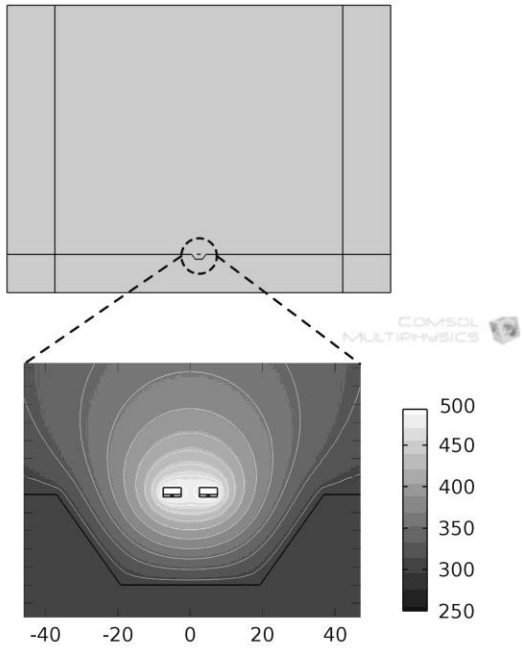

Figure 14

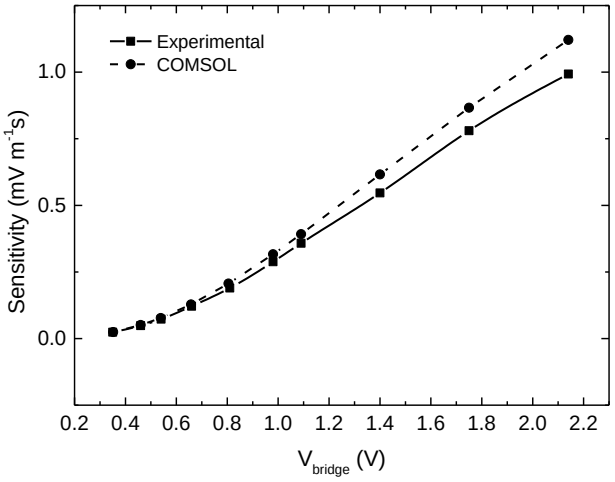

Figure 15

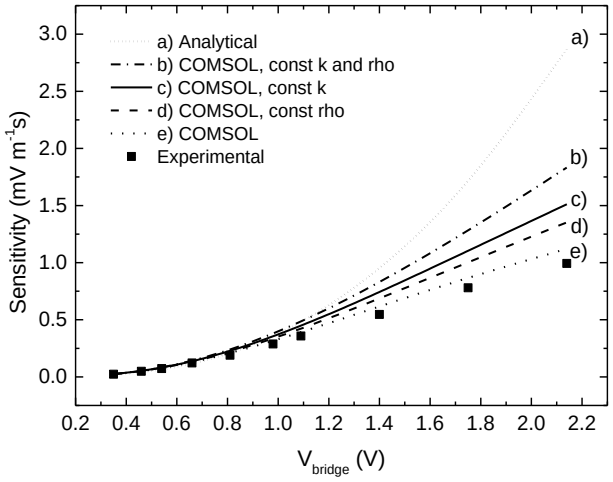

Figure 16